Al_2O_3 support triggering highly efficient photoreduction of CO_2 with H_2O on noble-metal-free $CdS/Ni_9S_8/Al_2O_3$

Sha Li[a,1], Qianqian Wang[b,1], Xiaoliang Yan[c,*], Hua-Qiang Zhuang[d], Chen Yuan[c], Junpeng Feng[c], Meijun Wang[c], Ruifeng Li[c], Wenyang Li[e], Yun-Xiang Pan[b,*]

[a] College of Textile Engineering, Taiyuan University of Technology, Taiyuan 030024, PR China
[b] Department of Instrument Science and Engineering, School of Electronic Information and Electrical Engineering, Shanghai Jiao Tong University, Shanghai 200240, PR China
[c] College of Chemistry and Chemical Engineering, Taiyuan University of Technology, Taiyuan 030024, PR China
[d] College of Chemical Engineering and Materials Science, Quanzhou Normal University, Quanzhou 362000, PR China
[e] School of Mechanical and Power Engineering, Dalian Ocean University, Dalian 116023, PR China

ABSTRACT

Noble-metal-free photocatalysts are promising for economic and efficient conversion of solar energy into chemical energies. Herein, a highly efficient CO evolution, with an evolution rate of $12.1\,\mu mol\,h^{-1}$, is achieved from the visible-light-driven photoreduction of CO_2 with H_2O on a noble-metal-free $CdS/Ni_9S_8/Al_2O_3$ photocatalyst. The CO evolution on $CdS/Ni_9S_8/Al_2O_3$ is comparable to that on the noble-metal-based $CdS/Pt/Al_2O_3$ photocatalyst ($10.6\,\mu mol\,h^{-1}$), but 11 times higher than that on the Al_2O_3-free CdS/Ni_9S_8 ($1.1\,\mu mol\,h^{-1}$) photocatalyst. The Al_2O_3 support facilitates the separation of the photogenerated electron-hole pairs, CO_2 adsorption and production of protons for reducing CO_2, thus enhancing the CO evolution. These results will open a new door for rationally fabricating efficient noble-metal-free photocatalysts, and favor the transition to solar energy economy.

1. Introduction

Solar-energy-driven photoreduction of CO_2 is promising for solving both the energy and environmental crises [1,2]. Yet, to date, the photoreduction efficiency is still far below the requirement of commercialization. The photoreduction efficiency is limited by the poor ability of the photocatalysts in separating the photogenerated electron-hole pairs, adsorbing CO_2 and producing protons for reducing CO_2 [3,4]. As such, the photocatalysts with enhanced electron-hole separation, CO_2 adsorption and proton production are highly desired.

Al_2O_3 has been extensively used as the catalyst support in conventional catalysis, where heating was used to provide the energy for driving the catalytic reactions, in both lab research and industrial applications [5–10]. Murata et al. observed that the efficiency of the Pd/Al_2O_3 catalyst in methane combustion is closely related to the Pd-Al_2O_3 interaction [5]. Zhu et al. reported that a stronger Ni-Al_2O_3 interaction efficiently enhance the coke-resistance, activity, selectivity and stability of the Ni/Al_2O_3 catalyst in the CO_2 reforming of methane [6]. During the selective acetylene hydrogenation, highly dispersed bimetallic Pd-In

catalyst supported on Al_2O_3 exhibited several magnitudes higher activity than the unsupported catalyst [7]. The oxygen vacancies and hydroxyl groups on Al_2O_3 were found to be benefit for improving the adsorption, activation and conversion of CO_2 on the Al_2O_3-supported catalysts [8]. Through both experimental and theoretical calculations, Foppa et al. implied that the Ni-Al_2O_3 interface provides the energetically favorable reaction pathway for CO_2 conversion on the Ni/Al_2O_3 catalyst [9]. In contrast to the wide applications in conventional catalysis, the application of Al_2O_3 in photocatalysis has not been well explored yet.

Cocatalysts are crucial for the photoreduction of CO_2 [11–15]. They provide the catalytically active sites for reducing CO_2. Noble metals, e.g. Pt, are the most widely used cocatalysts for the photoreduction of CO_2. They indeed result in significantly enhanced photoreduction efficiency. However, due to the limited abundance and high price, the noble metals are unsuitable for massive-scale applications. Low-cost noble-metal-free transition metal sulfides, such as nickel sulfides, are of particular interest for substituting the noble metals for the photoreduction of CO_2 [16–21]. In the sulfides, the electronic structure of the transition

metal is modified by the inclusion of the sulfur interstitial atoms *via* charge transfer or/and structural change, making the sulfides similar to noble metals. Besides, the sulfides are highly active towards the dissociation of the O−H and C=O bonds, which are the key steps in the photoreduction of CO_2. The performance of the sulfides in the photoreduction of CO_2 has been examined. For example, a CH_3OH evolution rate of about $1.0\,\mu mol\,h^{-1}$ was obtained from the photoreduction of CO_2 on Bi_2S_3/CdS [19], and Takayama et al. found that $CuGaS_2$ was active towards the photoreduction of CO_2 into CO, with a CO evolution rate of $0.15\,\mu mol\,h^{-1}$ [20]. However, the photoreduction efficiency of the sulfides is still very low, and requires further improvement.

Herein, we demonstrate that a highly efficient CO evolution, with an evolution rate of $12.1\,\mu mol\,h^{-1}$, can be achieved from the photoreduction of CO_2 with H_2O on a noble-metal-free $CdS/Ni_9S_8/Al_2O_3$ photocatalyst, under the irradiation of visible light ($\lambda > 420\,nm$) which is the main part of sunlight. The CO evolution rate on $CdS/Ni_9S_8/Al_2O_3$ is comparable to that on the noble-metal-based $CdS/Pt/Al_2O_3$ photocatalyst ($10.6\,\mu mol\,h^{-1}$), but 11 times higher than that on the Al_2O_3-free CdS/Ni_9S_8 ($1.1\,\mu mol\,h^{-1}$) photocatalyst. The Al_2O_3 support triggers improved separation of the photogenerated electron-hole pairs, CO_2 adsorption and production of protons for reducing CO_2. This is responsible for the enhanced CO evolution on $CdS/Ni_9S_8/Al_2O_3$.

2. Experimental

2.1. Sample preparation

All the reagents used herein were of analytical grade purity and were used as received without further treatment.

For fabricating Ni_9S_8/Al_2O_3, MIL-110 (Al) was firstly synthesized hydrothermally in the presence of trimethyl 1,3,5-benzenetricarboxylate (Me_3btc) [21]. MIL-110 (Al) is one of the metal-organic frameworks (MOFs) which are promising templates for forming catalysts *via* calcinations [22–24]. The porous structures of the catalysts prepared by using MOFs as the templates are similar to those of the MOF templates. This is benefit for achieving a high dispersion of the metal nanoparticles, even at a high metal content. The preparation of MIL-110 (Al) proceeded through the following steps. In the first step, 1.426 g of Al $(NO_3)_3·9H_2O$ (Tianjin Kermel Chemical Reagent Co., Ltd, AR, > 99.0%) was dissolved into 22 ml of deionized (DI) water. In the second step, 0.478 g of Me_3btc was added into the solution obtained in the first step under vigorous stirring. In the third step, 2.2 ml of NaOH (4 M) was introduced to form a white emulsion, followed by adding HNO_3 (4 M) to adjust the pH value to about 3.9. After stirring for another 30 min, the mixture obtained in the third step was transferred to a Teflon-lined stainless steel at 200 °C for 3 h. The sample obtained from the hydrothermal process was washed with DI water and further purified by dimethyl formamide (DMF, Tianjin Kermel Chemical Reagent Co., Ltd, AR, > 99.5%). The product was thoroughly washed with ethanol for several times to remove DMF and filtered, and dried at 80 °C for 12 h, leading to the formation of the yellowish powdered MIL-110 (Al). Fig. S1 in the Supplementary Data shows the XRD and SEM results of MIL-110 (Al). The MIL-110 (Al) exhibits a rod-like morphology and a XRD pattern characteristic of MOF.

Incipient wetness impregnation was used to load nickel precursor into MIL-110 (Al). Typically, 3.78 g of $Ni(NO_3)_2·6H_2O$ (Sinopharm chemical Reagent Co. Ltd., AR, > 98.0%) was dissolved in a DMF solution. 5 g of MIL-110 (Al) was then impregnated with the Ni-contained DMF solution for 12 h. As-obtained sample was dried at 120 °C for 12 h.

The Ni-impregnated MIL-110 (Al) was next sulfured in a fixed-bed tubular reactor. In the first step of the sulfuration, the temperature of the reactor was increased to 350 °C in N_2 with a flowing rate of 20 ml min^{-1}. And then, the N_2 was stopped, and H_2 containing dimethyl sulfide (CH_3SCH_3) as the sulfur source was introduced into the reactor (15 ml min^{-1}). A syringe pump was used to inject the CH_3SCH_3 liquid into the H_2 stream (0.5 ml min^{-1}). The sulfuration proceeded for 6 h.

After sulfuration of 6 h, the temperature of the reactor was decreased to room temperature in N_2 (20 ml min^{-1}), producing Ni_9S_8/Al_2O_3. For comparison, we also prepared Ni_9S_8/Al_2O_3 by using the thiophene, carbon disulfide and dimethyl disulfide as the sulfur sources through the process same as that by using the dimethyl sulfide.

For comparison, NiO/Al_2O_3 was prepared by calcining the Ni-impregnated MIL-110 (Al) in air at 400 °C for 3 h, and Ni/Al_2O_3 was fabricated by the same procedure as the sulfuration but only with hydrogen for reduction and without the addition of sulfide species.

Loading of CdS nanoparticles on Ni_9S_8/Al_2O_3, denoted as $CdS/Ni_9S_8/Al_2O_3$, was proceeded in 200 ml of aqueous solution containing 10 vol% triethanoamine (TEOA) as the sacrificial reagent. Ni_9S_8/Al_2O_3 (160 mg) and CdS nanoparticles (40 mg) were added into the solution under ultrasonication for 2 h. The mixture was then divided into two parts. One part (100 mL) was centrifuged to collect the solid sample which was washed with ethanol and DI water for several times and subsequently dried in a vacuum freeze drier for further characterization. The other part (100 mL) was used for the visible-light-driven photoreduction of CO_2 with H_2O.

For preparing CdS/Pt, the CdS nanoparticles (20 mg) were dispersed in 1 ml of water solution of $H_2PtCl_6·6H_2O$, with a Pt content of $2.0\,mg\,mL^{-1}$, under ultrasonication for 30 min, depositing Pt ions onto the CdS nanoparticles. And then, the sample was irradiated for 1 h by using a 300 W Xe-lamp, reducing Pt ions into Pt^0. Finally, the solid sample was harvested by centrifugation, washed with ethanol and DI water for several times, and dried under vacuum at 25 °C for 12 h, fabricating CdS/Pt.

2.2. Characterizations

The X-ray diffraction (XRD) patterns were recorded on an X' Pert Pro diffractometer equipped with Cu Kα radiation (scanning rate: 4° min^{-1}). An ASAP 2020 analyzer (Micromeritics, Norcross, GA, USA) was used to explore the Brunauer-Emmett-Teller (BET) surface areas. UV–vis spectra were obtained on a UV-3101 Shimadzu spectrophotometer. The X-ray photoelectron spectroscopy (XPS) was carried out on an ESCALAB250Xi X-ray photoelectron spectrometer with a monochromatic X-ray source manufactured by Thermo. The binding energy was calibrated using the C 1 s peak (284.6 eV). Transmission electron microscopy (TEM) observations, including high-resolution TEM (HRTEM) and elemental mapping, were performed on a Philips TECNAI G^2F30 system (beam energy: 200 kV). The Fourier transform infrared spectroscopy (FTIR) measurements were conducted on a Bruker Tensor-27 spectrometer (resolution: 4 cm^{-1}). A Fluoromax-3 spectrometer (Horiba Scientific) was used to collect the photoluminescence (PL) spectra. The inductively coupled plasma mass spectrometry (ICP-MS) measurements were conducted on a Thermo X series 2 ICP-MS spectrometer. A Bruker EMXplus-10/12 spectrometer was applied for obtaining the electron spin resonance (ESR) spectra, with a microwave frequency of 9.64 GHz and a modulation amplitude of 2 G. 5,5-dimethyl-1-pyrroline N-oxide (DMPO, ≥98.0%; Sigma Chemical Co.) was used as the spin-trap reagent for the hydroxyl radicals.

Transient photocurrents were measured on a CHI660 A electrochemical workstation in a Na_2SO_4 solution (0.1 M) containing TEOA (10 vol %), by using a 300 W Xe-lamp equipped with a cut-off filter ($\lambda > 420\,nm$), with a constant potential of 0.35 V *vs.* standard electrode (SCE). The solution and light source used for measuring the photocurrent are similar to those for the photocatalytic reactions. The workstation includes three electrodes. The working electrode, with a surface area of $1.44\,cm^2$ exposed to the electrolyte, was prepared by placing the sample on indium tin oxide (ITO) glasses. Pt and a saturated calomel electrode were used as the counter electrode and reference electrode, respectively. For preparing the working electrode, with a surface area of $1.44\,cm^2$ exposed to the electrolyte, 1 mg sample was firstly dispersed in 1 ml ethanol containing naphthol (0.05 wt%) under

ultrasonication. Then, the suspension was dropped onto ITO glasses, and dried at room temperature. The CO_2 adsorption capacities of the samples were examined on an ASAP 2020 analyzer (Micromeritics, Norcross, GA, USA), with pressures ranging from 0 to 1.01 bar, at 25 °C. Before the adsorption experiments, the samples were degassed at 200 °C for 12 h.

2.3. Photoreduction of CO_2 with H_2O

The photoreduction was performed in a closed gas circulation-evacuation reactor, with H_2O as the reductant, under the irradiation of visible light ($\lambda > 420$ nm). Before reaction, the following three steps were carried out. Firstly, 100 mg photocatalyst was dispersed in a H_2O solution (100 mL) containing TEOA (10 vol%) which serve as sacrificial reagents for capturing the photogenerated holes, in the reactor. And then, the reactor was evacuated and refilled with pure CO_2 gas for three times to remove the air inside. Finally, the reactor was filled with CO_2 until the pressure of the reactor reaching to the atmospheric pressure (101.325 kPa). In the photocatalytic reduction, the reactor was irradiated with a Xe-lamp (300 W) equipped with a cut-off filter ($\lambda > 420$ nm) under stirring, and the temperature of the reactor was kept at 25 °C by using cooling water. The products were detected by a gas chromatography (Agilent 7890 A) with both with Flame Ionization (FID) and Thermal Conductivity (TCD) detectors. The FID detector and an Agilent HPPLOT Q capillary column were used for analyzing methanol, while the TCD detector and a Porapak Q packed column were used for analyzing H_2, O_2, CO_2, CO and CH_4. Ar was used as the carrier gas. The GC was switched between the two columns by using a four-port valve. To determine the source of the carbon in the products, an isotopic experiment was carried out under the identical reaction conditions using $^{13}CO_2$ (99.99% in purity), and the products were analyzed by a gas chromatography-mass spectrometry (GC–MS).

3. Results

3.1. Ni_9S_8/Al_2O_3

Fig. 1a shows the XRD pattern of Ni_9S_8/Al_2O_3. On the XRD pattern, all of the peaks are attributed to the orthorhombic Ni_9S_8 (PDF#22-1193). There is no XRD peak assigned to Al_2O_3 for Ni_9S_8/Al_2O_3, indicating that the Al_2O_3 support is amorphous. Fig. 1b and c illustrate the N_2 absorption-desorption curves and pore size distribution for Ni_9S_8/Al_2O_3. From the N_2 absorption-desorption experiment, the BET surface area of Ni_9S_8/Al_2O_3 is calculated to be 143 $m^2 g^{-1}$.

The XPS spectra of the Ni and S on Ni_9S_8/Al_2O_3 are shown in Fig. S2 in the Supplementary Data. Six peaks at 853.1, 856.2, 861.4, 870.3, 873.8 and 880.2 eV, respectively, are present on the XPS spectrum of Ni (Fig. S2a). The peaks at 853.1, 856.2 and 870.3 eV are attributed to the $2p_{3/2}$, $2p_{3/2}$ and $2p_{1/2}$ of Ni in Ni_9S_8, respectively [25–27]. The peaks at 861.4, 873.8 and 880.2 eV are caused by the Ni in Ni-O bonds [25,26]. The XPS peak of S can be fitted into peaks at 161.3, 162.0, 162.7, 163.6, 166.3 and 168.2 eV, respectively (Fig. S2b). The peaks at 161.3 and 166.3 eV are assigned to the $2p_{1/2}$ of S in Ni_9S_8, and the peaks at 162.0, 162.7 and 163.6 eV are due to the $2p_{3/2}$ of S in Ni_9S_8 [25–27]. The peak at 168.2 eV is caused by the S in the S–O bonds [28–30]. The XPS results indicate that, besides the Ni-S bonds in Ni_9S_8, there are also Ni-O and S–O bonds on Ni_9S_8/Al_2O_3. The Ni-O and S–O bonds could be formed through the bonding interactions of the Ni and S atoms in Ni_9S_8 with the O atoms on the Al_2O_3 support, and could be the main drive to anchor Ni_9S_8 on the Al_2O_3 support.

Fig. 2a and b illustrate the TEM images of Ni_9S_8/Al_2O_3. The Ni_9S_8 nanoparticles are dispersed on the Al_2O_3 support. The lattice fringes with distances of 0.183 and 0.237 nm are due to the (115) and (330) planes of the orthorhombic Ni_9S_8, respectively, indicating the presence of the orthorhombic Ni_9S_8 on Ni_9S_8/Al_2O_3. This is in good agreement with the XRD and XPS results.
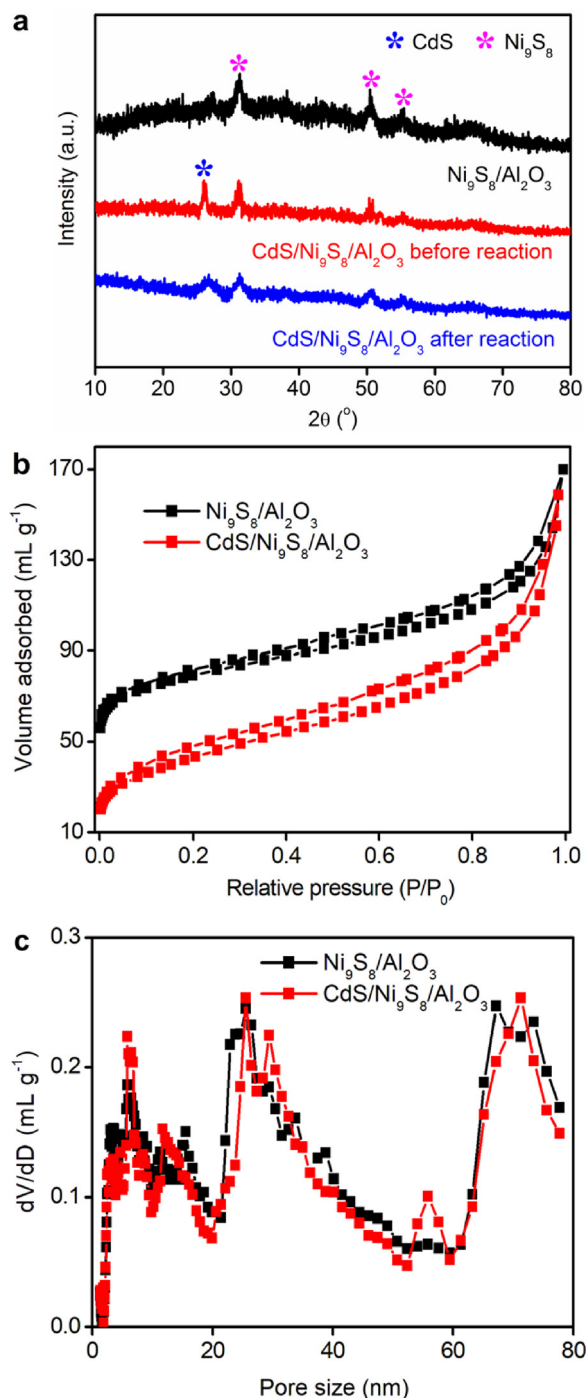
Fig. 1. (a) XRD patterns for Ni_9S_8/Al_2O_3, $CdS/Ni_9S_8/Al_2O_3$ before reaction and $CdS/Ni_9S_8/Al_2O_3$ after reaction. (b) N_2 adsorption-desorption curves and (c) pore size distributions for Ni_9S_8/Al_2O_3 and $CdS/Ni_9S_8/Al_2O_3$.

3.2. $CdS/Ni_9S_8/Al_2O_3$

CdS nanoparticles with an average size of about 5 nm (Fig. S3 in the Supplementary Data) were next loaded on Ni_9S_8/Al_2O_3 to form the $CdS/Ni_9S_8/Al_2O_3$ photocatalyst. The CdS nanoparticles in the cubic phase of CdS (Fig. S3) were fabricated via the hot-injection method which has been reported in detail elsewhere [31–33]. On the XRD pattern of $CdS/Ni_9S_8/Al_2O_3$ (Fig. 1a), besides the peaks of the orthorhombic Ni_9S_8, a peak at 26.5° assigned to the (111) plane of the cubic CdS also appears (PDF#80-0019). Fig. 2c–e show the HRTEM image and elemental mapping patterns for $CdS/Ni_9S_8/Al_2O_3$. The lattice fringe
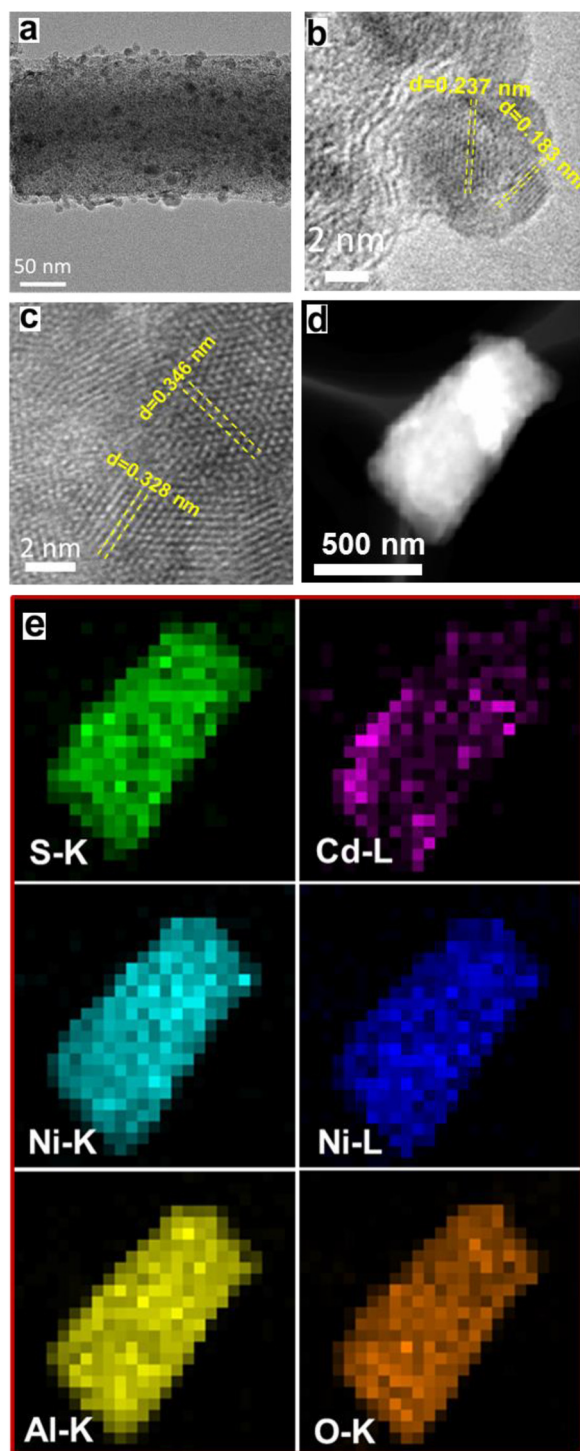
Fig. 2. (a) TEM and (b) HRTEM images of Ni_9S_8/Al_2O_3. (c) HRTEM image and (d, e) elemental mapping patterns of $CdS/Ni_9S_8/Al_2O_3$.

with a distance of 0.328 nm is attributed to the (202) plane of the orthorhombic Ni_9S_8, while the lattice fringe with a distance of 0.346 nm is caused by the (111) plane of the cubic CdS. Elemental mapping patterns evidence the presence of Ni, Cd, S, Al and O on $CdS/Ni_9S_8/Al_2O_3$. The UV–vis spectrum of $CdS/Ni_9S_8/Al_2O_3$ has an absorption edge of about 500 nm, which is similar to that of the pure CdS nanoparticles (Fig. S4 in the Supplementary Data) [31–33]. The ICP-MS measurements indicate that the contents of CdS, Ni_9S_8 and Al_2O_3 in $CdS/Ni_9S_8/Al_2O_3$ are 20 wt%, 23 wt% and 57 wt%, respectively. The BET surface area of $CdS/Ni_9S_8/Al_2O_3$ was measured to be $130\,m^2\,g^{-1}$, which is slightly
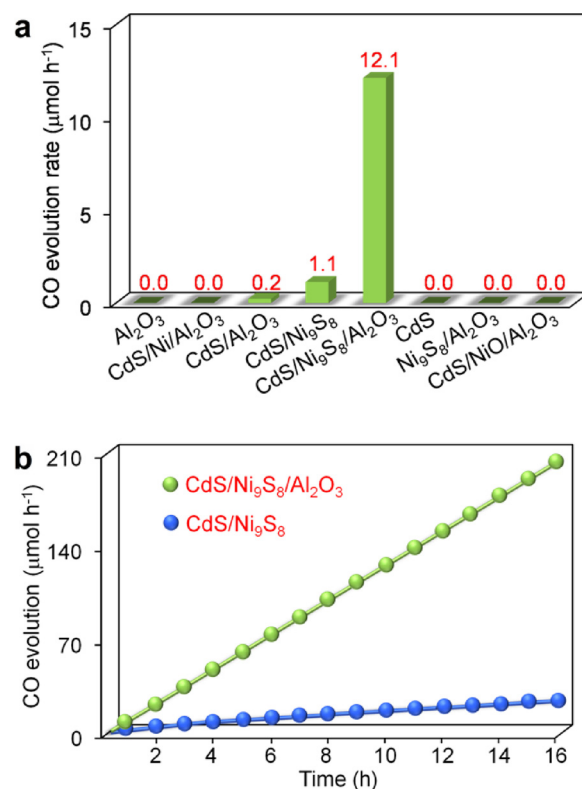

Fig. 3. (a) CO evolution rate in the visible-light-driven photoreduction of CO_2 with H_2O on Al_2O_3, $CdS/Ni/Al_2O_3$, CdS/Al_2O_3, CdS/Ni_9S_8, $CdS/Ni_9S_8/Al_2O_3$, CdS, Ni_9S_8/Al_2O_3 and $CdS/NiO/Al_2O_3$. (b) Stability of $CdS/Ni_9S_8/Al_2O_3$ and CdS/Ni_9S_8 in the visible-light-driven photoreduction of CO_2 with H_2O. Reaction conditions: 100 ml water solution containing 10 vol% TEOA, 100 mg photocatalyst, 300 W Xe-lamp ($\lambda > 420$ nm).

smaller than that of Ni_9S_8/Al_2O_3 (Fig. 1b). The pore size distribution of $CdS/Ni_9S_8/Al_2O_3$ is similar to that of Ni_9S_8/Al_2O_3 (Fig. 1c).

3.3. Photoreduction of CO_2 with H_2O

The performance of $CdS/Ni_9S_8/Al_2O_3$ and control samples in the visible-light-driven photoreduction of CO_2 with H_2O were next explored by using the aqueous solution containing TEOA (10 vol%) as a hole scavenger. The results are plotted in Fig. 3 and Fig. S5 in the Supplementary Data. During the experiments, CO is the main the product. In addition to CO, there is some methanol detected during the photocatalytic reactions, but the evolution rate of the methanol is lower than $0.1\,\mu mol\,h^{-1}$. As reflected in Figs. 3a and S5, Al_2O_3, CdS, Ni/Al_2O_3, NiO/Al_2O_3 and Ni_9S_8/Al_2O_3 are not active towards the photoreduction. CO evolution is observed on CdS/Al_2O_3 and CdS/Ni_9S_8, but the evolution rates are only 0.2 and $1.1\,\mu mol\,h^{-1}$, respectively. By exploring the influence of the amount of the $Ni(NO_3)_2\cdot 6H_2O$ and CdS for preparing the photocatalysts (Table S1 in the Supplementary Data), the CO evolution rates on $CdS/NiO/Al_2O_3$ and $CdS/Ni/Al_2O_3$ were found to be zero.

After examining the influences of the amount of the CdS nanoparticles and the sulfur source for preparing $CdS/Ni_9S_8/Al_2O_3$ on the photocatalytic activity (Figs. S6 and S7 in the Supplementary Data), an optimum CO evolution rate of $12.1\,\mu mol\,h^{-1}$ was obtained on $CdS/Ni_9S_8/Al_2O_3$, which is 11 times higher than that on CdS/Ni_9S_8. In addition to CO, H_2 and O_2 are also detected in the photoreduction of CO_2 with H_2O on $CdS/Ni_9S_8/Al_2O_3$, with evolution rates of 84.1 and $37.3\,\mu mol\,h^{-1}$, respectively. We also compared the activity of $CdS/Ni_9S_8/Al_2O_3$ with the noble-metal-based $CdS/Pt/Al_2O_3$ photocatalyst. By varying the amount of CdS and Pt on $CdS/Pt/Al_2O_3$ (Fig. S8 in the

Supplementary Data), an optimum CO evolution rate of 10.6 μmol h^{-1} is observed on CdS/Pt/Al$_2$O$_3$. As such, the photocatalytic activity of CdS/Ni$_9$S$_8$/Al$_2$O$_3$ is comparable to that of CdS/Pt/Al$_2$O$_3$, and the noble-metal-free Ni$_9$S$_8$ is a good alternative to Pt to be used as cocatalysts in the photoreduction of CO$_2$. CdS/Ni$_9$S$_8$/Al$_2$O$_3$ exhibits a better photocatalytic stability than CdS/Ni$_9$S$_8$. As shown in Fig. 3b, the CO evolution rate on CdS/Ni$_9$S$_8$/Al$_2$O$_3$ is almost unchanged during the light irradiation of 16 h, whereas the CO evolution rate on CdS/Ni$_9$S$_8$ becomes zero after light irradiation of 10 h. These results demonstrate that the Al$_2$O$_3$ support triggers an enhanced photoreduction of CO$_2$ with H$_2$O to produce CO.

For exploring the carbon source of the CO produced on CdS/Ni$_9$S$_8$/Al$_2$O$_3$, three control experiments (**Ex.**) were done, including: (i) **Ex.** with CdS/Ni$_9$S$_8$/Al$_2$O$_3$, CO$_2$ and H$_2$O, but without light; (ii) **Ex.** with CO$_2$, H$_2$O and light, but without CdS/Ni$_9$S$_8$/Al$_2$O$_3$; (iii) **Ex.** with CdS/Ni$_9$S$_8$/Al$_2$O$_3$, light and H$_2$O, but without CO$_2$. No CO is generated in all of the **Ex.**, implying that CO is from the visible-light-driven photoreduction of CO$_2$ with H$_2$O on CdS/Ni$_9$S$_8$/Al$_2$O$_3$. Besides, an isotopic experiment with ^{13}CO$_2$ as the reactant was also done for determining the source of the carbon in CO. The m/z at 29 on the GC–MS spectrum is caused by ^{13}CO (Fig. S9 in the Supplementary Data), further revealing that CO is from the visible-light-driven photoreduction of CO$_2$ with H$_2$O on CdS/Ni$_9$S$_8$/Al$_2$O$_3$.

4. Discussions

4.1. Roles of CdS, Ni$_9$S$_8$ and Al$_2$O$_3$ in the photoreduction

During the photoreduction of CO$_2$, the CdS nanoparticles are responsible for the absorption of the visible light, as indicated by the UV–vis spectra (Fig. S4). The Ni$_9$S$_8$ nanoparticles play as the cocatalysts providing the active sites for the photocatalytic reactions, as reflected by the low CO evolution on CdS/Al$_2$O$_3$ (Fig. 3a) as well as the comparable CO evolution on CdS/Ni$_9$S$_8$/Al$_2$O$_3$ to that on CdS/Pt/Al$_2$O$_3$. The much higher CO evolution on CdS/Ni$_9$S$_8$/Al$_2$O$_3$ than that on CdS/Ni$_9$S$_8$ suggests that the Al$_2$O$_3$ support plays an important role in the visible-light-driven photoreduction of CO$_2$ with H$_2$O. For investigating the role of the Al$_2$O$_3$ support, we studied the ability of the photocatalysts in separating the photogenerated electron-hole pairs, adsorbing CO$_2$ and producing protons from H$_2$O splitting, which are the key factors affecting the photoreduction efficiency of CO$_2$.

Fig. 4a plots the PL spectra of CdS, CdS/Ni$_9$S$_8$ and CdS/Ni$_9$S$_8$/Al$_2$O$_3$. An evident peak at 490 nm, which is assigned to the recombination of the photogenerated electron-hole pairs, appears on the PL spectrum of CdS. This is in good agreement with the PL results reported previously for CdS [31–34]. On CdS/Ni$_9$S$_8$ and CdS/Ni$_9$S$_8$/Al$_2$O$_3$, the PL peak at 490 nm is quenched significantly, implying an efficient electron-hole separation. The photocurrents of CdS, CdS/Ni$_9$S$_8$ and CdS/Ni$_9$S$_8$/Al$_2$O$_3$ are illustrated in Fig. 4b. The photocurrent on CdS/Ni$_9$S$_8$/Al$_2$O$_3$ is 0.42 mA cm^{-2}, which is much higher than those on CdS/Ni$_9$S$_8$ (0.33 mA cm^{-2}) and CdS (0.02 mA cm^{-2}). Thus, on CdS/Ni$_9$S$_8$/Al$_2$O$_3$, the electron-hole recombination is efficiently suppressed, and more photogenerated electrons are transferred into the measuring circuit during the photocurrent experiments. The PL and photocurrent results indicate that the Al$_2$O$_3$ support triggers more efficient electron-hole separation during the photocatalytic reaction. As reported previously, in photocatalysis, highly conductive supports, such as reduced graphene oxide and carbon nanotubes, can efficiently promote the separation of the photogenerated electron-hole pairs [18,35–37]. Our present results suggest that the Al$_2$O$_3$ support, which has a poor conductivity, is also excellent in separating the photogenerated electron-hole pairs. This could be originated from the defects and the hydroxyl groups on the Al$_2$O$_3$ support.

Fig. 5a plots the CO$_2$ adsorption capacity of CdS, Ni$_9$S$_8$, Al$_2$O$_3$, CdS/Ni$_9$S$_8$, Ni$_9$S$_8$/Al$_2$O$_3$ and CdS/Ni$_9$S$_8$/Al$_2$O$_3$. The CO$_2$ adsorption capacity of CdS/Ni$_9$S$_8$/Al$_2$O$_3$ is 1.53 mmol g^{-1}, which is higher than those of
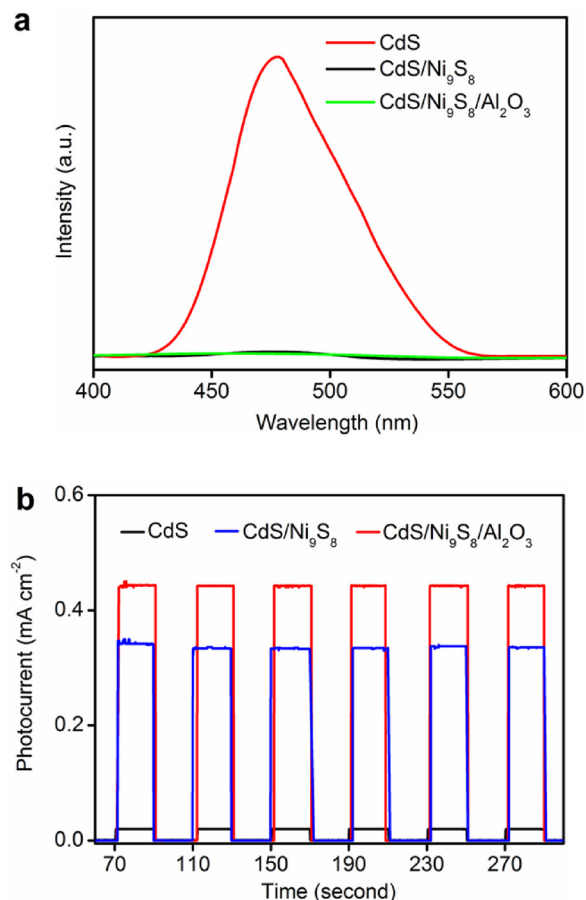
Fig. 4. (a) PL spectra and (b) photocurrent-time profiles for CdS, CdS/Ni$_9$S$_8$ and CdS/Ni$_9$S$_8$/Al$_2$O$_3$.

CdS (0.12 mmol g^{-1}), Ni$_9$S$_8$ (0.49 mmol g^{-1}) and Al$_2$O$_3$ (1.15 mmol g^{-1}). The CO$_2$ adsorption capacity of CdS/Ni$_9$S$_8$/Al$_2$O$_3$ is about 2.5 and 1.1 times higher than those on CdS/Ni$_9$S$_8$ (0.62 mmol g^{-1}) and Ni$_9$S$_8$/Al$_2$O$_3$ (1.40 mmol g^{-1}), respectively. The interface and synergetic effect among different components may enhance the CO$_2$ adsorption on CdS/Ni$_9$S$_8$/Al$_2$O$_3$. We have explored the O 1 s XPS spectrum of Ni$_9$S$_8$/Al$_2$O$_3$, as shown in Fig. S10 in the Supplementary Data. The XPS peaks at 530.9, 531.8, and 532.7 eV are attributed to the O^{2-} ion in the Al$_2$O$_3$ structure (O$_a$), oxygen vacancies (O$_b$) and near-surface oxygen (O$_c$), respectively [38]. The ratio of O$_b$ to the total oxygen species is 44% based on the calculation of O$_b$/(O$_a$ + O$_b$ + O$_c$). The oxygen vacancies could also make some contributions to the enhanced CO$_2$ adsorption on CdS/Ni$_9$S$_8$/Al$_2$O$_3$ [39]. As such, the Al$_2$O$_3$ support triggers an improved CO$_2$ adsorption on the photocatalyst.

Fig. 5b illustrates the dependence of the adsorption heat on the amount of CO$_2$ adsorbed, estimated by the Clausius-Clapeyron equation [40–42]. For all of the samples, the adsorption heat decreases with increasing CO$_2$ coverage, and the highest adsorption heat is obtained at the onset of CO$_2$ adsorption. For CdS, the highest adsorption heat is only 11.2 kJ mol^{-1}. With increasing the CO$_2$ adsorption coverage, the adsorption heat on CdS is close to zero. The low adsorption heat indicates that the CO$_2$ adsorption on CdS may be physical adsorption without any structural change occurring on the linear CO$_2$ molecule (O−C−O angle: 180°) [8]. The physical adsorption could be responsible for the low CO$_2$ adsorption capacity of CdS (Fig. 5a). The adsorption heats of Ni$_9$S$_8$ and CdS/Ni$_9$S$_8$ are similar, with the highest value of about 55.0 kJ mol^{-1}. The highest adsorption heat of CO$_2$ on Al$_2$O$_3$ is 65.0 kJ mol^{-1}, which is in good agreement with the adsorption heat obtained from the density functional theory (DFT) calculations in our previous papers [39,43,44]. The highest adsorption heat of CO$_2$ on
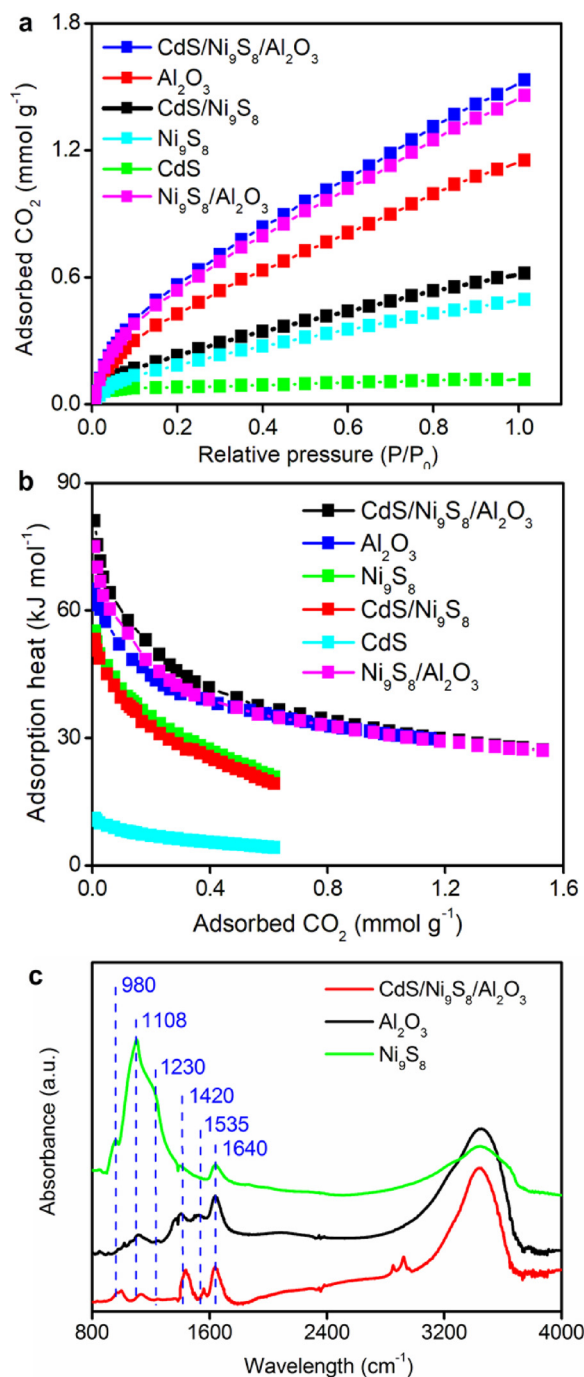
Fig. 5. (a) CO_2 adsorption capacity and (b) adsorption heat of CO_2 on CdS, Ni_9S_8, Al_2O_3, Ni_9S_8/Al_2O_3, CdS/Ni_9S_8 and $CdS/Ni_9S_8/Al_2O_3$. (c) FTIR spectra of CO_2 adsorption on Ni_9S_8, Al_2O_3 and $CdS/Ni_9S_8/Al_2O_3$.

$CdS/Ni_9S_8/Al_2O_3$ is $81.2\ kJ\ mol^{-1}$. The adsorption heat of CO_2 on $CdS/Ni_9S_8/Al_2O_3$ is enhanced as compared with those on CdS, Ni_9S_8 and Al_2O_3. This reveals the promotion effect of the interface and synergetic effect among different components on the CO_2 adsorption on $CdS/Ni_9S_8/Al_2O_3$. The adsorption heat of CO_2 on $CdS/Ni_9S_8/Al_2O_3$ is also enhanced as compared with those on CdS/Ni_9S_8 and Ni_9S_8/Al_2O_3. This suggests that the Al_2O_3 support triggers an improved CO_2 adsorption on the photocatalyst. These results are in good agreement with the CO_2 adsorption capacity measurements (Fig. 5a). As plotted in Fig. 5b, when the CO_2 adsorption coverage is higher than $0.8\ mmol\ g^{-1}$, the adsorption heat of CO_2 on $CdS/Ni_9S_8/Al_2O_3$ is close to that on Al_2O_3. As such, CO_2 could be adsorbed on the Al_2O_3 support with CO_2 adsorption

coverage higher than $0.8\ mmol\ g^{-1}$.

We next explored the products formed upon CO_2 adsorption on $CdS/Ni_9S_8/Al_2O_3$ through comparing the FTIR spectrum of CO_2 adsorption on $CdS/Ni_9S_8/Al_2O_3$ with those on Al_2O_3 and Ni_9S_8. As shown in Fig. 5c, on the FTIR spectra of CO_2 adsorption on Al_2O_3, Ni_9S_8 and $CdS/Ni_9S_8/Al_2O_3$, bands at 980, 1108, 1230, 1420, 1535 and $1640\ cm^{-1}$ appear. The bands at 980 and $1108\ cm^{-1}$ are assigned to the negatively charged CO_2^{-} species, with a bent structure in which the O−C−O angle is about 140° [39,43,44]. The bands at 1230 and $1420\ cm^{-1}$ are caused by the bidentate and monodentate carbonate species (CO_3^{2-}), respectively [8,39,43,44]. The bands at 1535 and $1640\ cm^{-1}$ are due to the bicarbonate species (HCO_3^{-}) formed from the protonation reaction between the carbonate species and the hydroxyl groups on the photocatalyst [8,39,43,44]. On the FTIR spectrum of Ni_9S_8, the bands due to the CO_2^{-} species dominate, whereas on the FTIR spectra of Al_2O_3 and $CdS/Ni_9S_8/Al_2O_3$, the main bands are those assigned to the carbonate and bicarbonate species. As such, the presence of the Al_2O_3 support triggers the formation of the carbonate and bicarbonate species from CO_2 adsorption. Previous DFT calculations demonstrated that, on the Al_2O_3-supported catalysts, the carbonate species are formed upon CO_2 adsorption, and then converted into bicarbonate species through protonation process in which the protons of the hydroxyl groups on the Al_2O_3 support are transferred to one of the oxygen atoms of the carbonate species [8,39,43,44]. The carbonate and bicarbonate species have been shown to be the key intermediates for CO_2 conversion [45–47]. Therefore, the formation of the carbonate and bicarbonate species resulted from the presence of the Al_2O_3 support could be one of the reasons for the enhanced CO evolution on $CdS/Ni_9S_8/Al_2O_3$ as compared with CdS/Ni_9S_8 without the Al_2O_3 support.

Fig. 6 shows the activity of the photocatalysts for producing hydrogen in the visible-light-driven photocatalytic H_2O splitting. There is no hydrogen evolution from Al_2O_3, $CdS/Ni/Al_2O_3$, Ni_9S_8/Al_2O_3 and $CdS/NiO/Al_2O_3$. Hydrogen was detected on CdS and CdS/Al_2O_3, but the evolution rates are only 3.6 and $5.4\ \mu mol\ h^{-1}$, respectively. On CdS/Ni_9S_8, the hydrogen production is enhanced, with an evolution rate of $30.8\ \mu mol\ h^{-1}$. As compared with CdS/Ni_9S_8, the hydrogen evolution rate on $CdS/Ni_9S_8/Al_2O_3$ increases further, with a value of $84.1\ \mu mol\ h^{-1}$. The quantum efficiency (QE) of $CdS/Ni_9S_8/Al_2O_3$ in hydrogen production is shown in Fig. 6b. With the wavelength increasing from 420 to 520 nm, the QE of $CdS/Ni_9S_8/Al_2O_3$ becomes higher firstly, and then decreases, with the highest QE (20.4%) presents at 460 nm. The photocatalytic stability of $CdS/Ni_9S_8/Al_2O_3$ was examined in four consecutive runs with each run of 4 h, and there is nothing to do but evacuate the reactor between two runs. As shown in Fig. 6c, $CdS/Ni_9S_8/Al_2O_3$ has a good stability in hydrogen production. There is almost no decrease of the total amount of the hydrogen produced after four runs on $CdS/Ni_9S_8/Al_2O_3$. These results show that the Al_2O_3 support triggers an enhanced hydrogen production (proton production) from the visible-light-driven photocatalytic H_2O splitting.

PL, photocurrent, CO_2 adsorption and hydrogen production experiments suggest that, in the visible-light-driven photoreduction of CO_2 with H_2O, the Al_2O_3 support triggers enhanced separation of the photogenerated electron-hole pairs, CO_2 adsorption and production of hydrogen (or proton) for reducing CO_2. This will definitely increase the amount of the electrons, CO_2 and hydrogen (or proton) participating in the photoreduction of CO_2, thus leading to the enhanced CO evolution from the photoreduction of CO_2 on $CdS/Ni_9S_8/Al_2O_3$.

4.2. Mechanism of the photoreduction

Reactions possibly occurring during the visible-light-driven photoreduction of CO_2 with H_2O to form CO on $CdS/Ni_9S_8/Al_2O_3$ are listed as Eqs. (1)–(9) (Eqs. (1)–(9)). Light absorption by $CdS/Ni_9S_8/Al_2O_3$ leads to the formation of the electron-hole pairs (Eq. (1)). Capture of the photogenerated holes by the TEOA produces $TEOA^{+}$ (Eq. (2)). H_2O can be split into an H atom and an OH^{-} in the presence of the
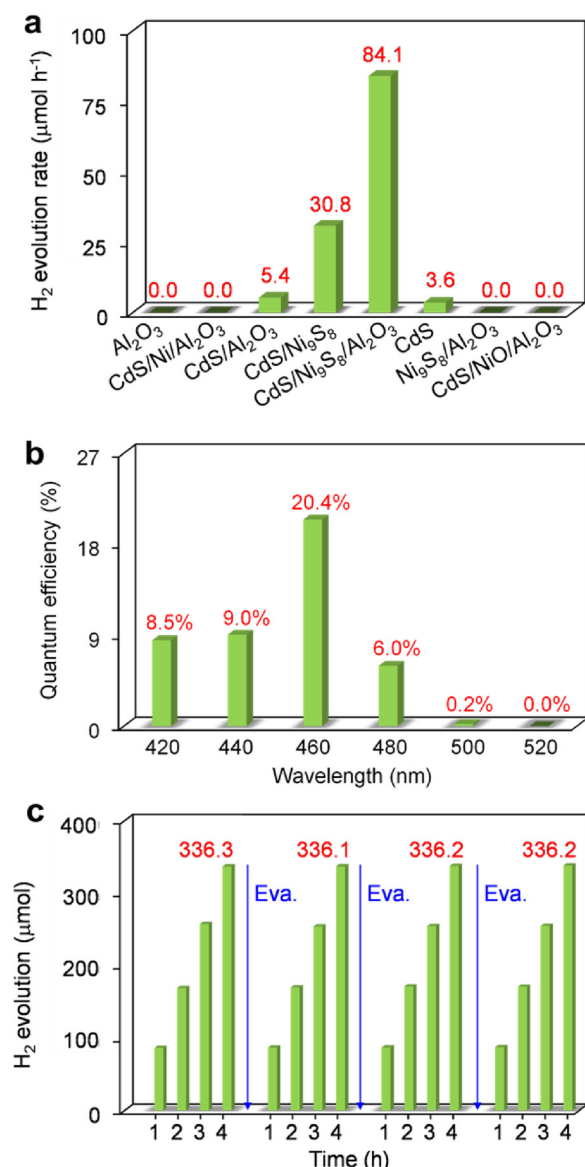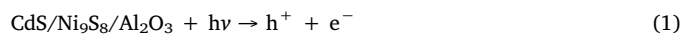
Fig. 6. (a) Hydrogen evolution rate in the visible-light-driven photocatalytic H_2O splitting on Al_2O_3, $CdS/Ni/Al_2O_3$, CdS/Al_2O_3, CdS/Ni_9S_8, $CdS/Ni_9S_8/Al_2O_3$, CdS, Ni_9S_8/Al_2O_3 and $CdS/NiO/Al_2O_3$. (b) QE values of $CdS/Ni_9S_8/Al_2O_3$ in hydrogen production from the visible-light-driven photocatalytic H_2O splitting. (c) Stability of $CdS/Ni_9S_8/Al_2O_3$ in the visible-light-driven photocatalytic H_2O splitting. Reaction conditions: 100 ml water solution containing 10 vol% TEOA, 100 mg photocatalyst, 300 W Xe-lamp (λ > 420 nm).

photogenerated electrons (Eq. (3)). Reaction of OH^- with $TEOA^+$ results in an OH group and a TEOA molecule (Eq. (4)). Reaction of CO_2 with the proton and photogenerated electron (Eq. (5)), or/and with the H atom (Eq. (6)), produces CO and an OH group. ESR experiments were conducted for studying the formation of the hydroxyl radicals by using DMPO as the radical probe. The evident DMPO-OH signals indicate the presence of the OH radicals (Fig. S11 in the Supplementary Data) [48]. The protons (or H atoms) can combine together to form H_2 (Eqs. (7) and (8)), and the OH groups can be converted into O_2 and H_2O (Eqs. (9)). During the conversion of CO_2 into CO through reactions 5 and 6, carbon and bicarbonate species could be the key intermediates. We analyzed the influence of the photoreduction on the photocatalyst by conducting XRD measurement. As shown in Fig. 1a, the XRD pattern of the photocatalyst after the photoreduction of 16 h is similar to that of the photocatalyst before the photoreduction. This indicates that there is almost no change on the properties of the photocatalyst.

$$CdS/Ni_9S_8/Al_2O_3 + h\nu \rightarrow h^+ + e^- \tag{1}$$

$$h^+ + TEOA \rightarrow TEOA^+ \tag{2}$$

$$H_2O + e^- \rightarrow H + OH^- \tag{3}$$

$$OH^- + TEOA^+ \rightarrow TEOA + OH \tag{4}$$

$$CO_2 + H^+ + e^- \rightarrow CO + OH \tag{5}$$

$$CO_2 + H \rightarrow CO + OH \tag{6}$$

$$2H^+ + 2e^- \rightarrow H_2 \tag{7}$$

$$2H \rightarrow H_2 \tag{8}$$

$$4OH \rightarrow 2H_2O + O_2 \tag{9}$$

The Ni/Al_2O_3 catalyst has been widely used in industry [49–51]. Sulfur poisoning, which can convert nickel into nickel sulfide, is one of the most serious problems negatively affecting the activity, selectivity and stability of the Ni/Al_2O_3 catalyst [49–51]. Generally, the sulfur-poisoned Ni/Al_2O_3 catalyst is discarded or regenerated through complex processes. Our present work indicates that the sulfur-poisoned Ni/Al_2O_3 catalyst could be excellent cocatalysts for the photoreduction of CO_2. This opens a new way for the application of the sulfur-poisoned Ni/Al_2O_3 catalyst.

5. Conclusions

In conclusion, a highly efficient CO evolution, with an evolution rate of 12.1 $\mu mol\,h^{-1}$, is achieved from the photoreduction of CO_2 with H_2O on a noble-metal-free $CdS/Ni_9S_8/Al_2O_3$ photocatalyst, under the irradiation of visible light (λ > 420 nm) which is the main part of sunlight. The CO evolution rate on $CdS/Ni_9S_8/Al_2O_3$ is comparable to that on the noble-metal-based $CdS/Pt/Al_2O_3$ photocatalyst (10.6 $\mu mol\,h^{-1}$), but 11 times higher than that on the Al_2O_3-free CdS/Ni_9S_8 (1.1 $\mu mol\,h^{-1}$) photocatalyst. The Al_2O_3 support triggers improved separation of the photogenerated electron-hole pairs, CO_2 adsorption and production of protons for reducing CO_2. This is responsible for the enhanced CO evolution on the $CdS/Ni_9S_8/Al_2O_3$. These results are helpful for fabricating low-cost noble-metal-free photocatalysts for more efficient photoreduction of CO_2.

Acknowledgements

Appendix A. Supplementary data

Supplementary material related to this article can be found, in the online version, at doi:https://doi.org/10.1016/j.apcatb.2018.08.060.

References

[1] Z.B. Liang, C. Qu, W.H. Guo, R.Q. Zou, Q. Xu, Pristine metal–organic frameworks and their composites for energy storage and conversion, Adv. Mater. 1702891 (2017) 1–39.
[2] S.B. Wang, X.C. Wang, Imidazolium ionic liquids, imidazolylidene heterocyclic carbenes, and zeolitic imidazolate frameworks for CO_2 capture and photochemical reduction, Angew. Chem. Int. Ed. 55 (2016) 2308–2320.
[3] A. Dhakshinamoorthy, A.M. Asiri, H. García, Metal–Organic Framework (MOF)

compounds: photocatalysts for redox reactions and solar fuel production, Angew. Chem. Int. Ed. 55 (2016) 5414–5445.

[4] X.G. Meng, L.Q. Liu, S.X. Ouyang, H. Xu, D.F. Wang, N.Q. Zhao, J.H. Ye, Nanometals for solar-to-chemical energy conversion: from semiconductor-based photocatalysis to plasmon-mediated photocatalysis and photo-thermocatalysis, Adv. Mater. 28 (2017) 6781–6803.

[5] K. Murata, Y. Mahara, J. Ohyama, Y. Yamamoto, S. Arai, A. Satsuma, The metal-support interaction concerning the particle size effect of Pd/Al$_2$O$_3$ on methane combustion, Angew. Chem. Int. Ed. 56 (2017) 15993–15997.

[6] X.L. Zhu, P.P. Huo, Y.P. Zhang, D.G. Cheng, C.J. Liu, Structure and reactivity of plasma treated Ni/Al$_2$O$_3$ catalyst for CO$_2$ reforming of methane, Appl. Catal. B: Environ. 81 (2008) 132–140.

[7] Y.Q. Cao, Z.J. Sui, Y. Zhu, X.G. Zhou, D. Chen, Selective hydrogenation of acetylene over Pd-In/Al$_2$O$_3$ catalyst: promotional effect of indium and composition-dependent performance, ACS Catal. 7 (2017) 7835–7846.

[8] Y.-X. Pan, C.J. Liu, Q.F. Ge, Adsorption and protonation of CO$_2$ on partially hydroxylated γ-Al$_2$O$_3$ surfaces: a density functional theory study, Langmuir 24 (2008) 12410–12419.

[9] L. Foppa, T. Margossian, S.M. Kim, C. Müller, C. Copéret, K. Larmier, A. Comas-Vives, Contrasting the role of Ni/Al$_2$O$_3$ interfaces in water–gas shift and dry reforming of methane, J. Am. Chem. Soc. 139 (2017) 17128–17139.

[10] A. Piovano, E. Morra, M. Chiesa, E. Groppo, Tuning the Ti^{3+} and Al^{3+} synergy in an Al$_2$O$_3$/TiCl$_x$ catalyst to modulate the grade of the produced polyethylene, ACS Catal. 7 (2017) 4915–4921.

[11] W.J. Ong, L.L. Tan, Y.H. Ng, S.T. Yong, S.P. Chai, Graphitic carbon nitride (g-C$_3$N$_4$)-based photocatalysts for artificial photosynthesis and environmental remediation: are we a step closer to achieving sustainability, Chem. Rev. 116 (2016) 7159–7329.

[12] F.Y. Wen, C. Li, Hybrid artificial photosynthetic systems comprising semiconductors as light harvesters and biomimetic complexes as molecular cocatalysts, Acc. Chem. Res. 46 (2013) 2355–2364.

[13] X.Q. Liu, J. Iocozzia, Y. Wang, X. Cui, Y.H. Chen, S.Q. Zhao, Z. Li, Z.Q. Lin, Noble metal–metal oxide nanohybrids with tailored nanostructures for efficient solar energy conversion, photocatalysis and environmental remediation, Energy Environ. Sci. 10 (2017) 402–434.

[14] C.M. Li, Y. Xu, W.G. Tu, G. Chen, R. Xu, Metal-free photocatalysts for various applications in energy conversion and environmental purification, Green Chem. 19 (2017) 882–899.

[15] Y.B. Huang, J. Liang, X.S. Wang, R. Cao, Multifunctional metal–organic framework catalysts: synergistic catalysis and tandem reactions, Chem. Soc. Rev. 46 (2017) 126–157.

[16] S. Navalón, A. Dhakshinamoorthy, M. Álvaro, H. Garcia, Photocatalytic CO$_2$ reduction using non-titanium metal oxides and sulfides, ChemSusChem 6 (2013) 562–577.

[17] S.N. Habisreutinger, L. Schmidt-Mende, J.K. Stolarczyk, Photocatalytic reduction of CO$_2$ on TiO$_2$ and other semiconductors, Angew. Chem. Int. Ed. 52 (2013) 7372–7408.

[18] A. Iwase, S. Yoshino, T. Takayama, Y.H. Ng, R. Amal, A. Kudo, Water splitting and CO$_2$ reduction under visible light irradiation using z-scheme systems consisting of metal sulfides, CoO$_x$-loaded BiVO$_4$, and a reduced graphene oxide electron mediator, J. Am. Chem. Soc. 138 (2016) 10260–10264.

[19] X. Li, J.T. Chen, H.L. Li, J.T. Li, Y.T. Xu, Y.J. Liu, J.R. Zhou, Photoreduction of CO$_2$ to methanol over Bi$_2$S$_3$/CdS photocatalyst under visible light irradiation, J. Nat. Gas Chem. 20 (2011) 413–417.

[20] T. Takayama, K. Sato, T. Fujimura, Y. Kojima, A. Iwase, A. Kudo, Photocatalytic CO$_2$ reduction using water as an electron donor by a powdered z-scheme system consisting of metal sulfide and an RGO–TiO$_2$ composite, Faraday Discuss. 198 (2017) 397–407.

[21] M. Haouas, C. Volkringer, T. Loiseau, G. Férey, F. Taulelle, The extra-framework sub-lattice of the metal–organic framework MIL-110: a solid-state NMR investigation, Chem. Eur. J. 15 (2009) 3139–3146.

[22] X. Yan, N. Lu, B. Fan, J. Bao, D. Pan, M. Wang, R. Li, Synthesis of mesoporous and tetragonal zirconia with inherited morphology from metal-organic frameworks, CrystEngComm 17 (2015) 6426–6433.

[23] P. Pachfule, D. Shinde, M. Majumder, Q. Xu, Fabrication of carbon nanorods and grapheme nanoribbons from a metal-organic framework, Nat. Chem. Biol. 8 (2016) 718–724.

[24] W. Cao, W. Luo, H. Ge, Y. Su, A. Wang, T. Zhang, UiO-66 derived Ru/ZrO$_2$@C as a highly stable catalyst for hydrogenation of levulinic acid to gamma-valerolactone, Green Chem. 19 (2017) 2201–2211.

[25] A. Khalil, Q. Liu, Z. Muhammad, M. Habib, R. He, Q. Khan, Q. Fang, H.T. Masood, Z. ur Rehman, T. Xiang, C.Q. Wu, L. Song, Synthesis of Ni$_9$S$_8$/MoS$_2$ heterocatalyst for enhanced hydrogen evolution reaction, Langmuir 33 (2017) 5148–5153.

[26] S.Z. Li, T. Chen, J. Wen, P.B. Gui, G.J. Fang, In situ grown Ni$_9$S$_8$ nanorod/O-MoS$_2$ nanosheet nanocomposite on carbon cloth as a free binder supercapacitor electrode and hydrogen evolution catalyst, Nanotechnology 28 (2017) 445407.

[27] W.Y. Wu, S. Chakrabortty, C.K.L. Chang, A. Guchhait, M. Lin, Y. Chan, Promoting 2D growth in colloidal transition metal sulfide semiconductor nanostructures via halide ions, Chem. Mater. 26 (2014) 6120–6126.

[28] L.L. Feng, G.T. Yu, Y.Y. Wu, G.D. Li, H. Li, Y.H. Sun, T. Asefa, W. Chen, X.X. Zou, High-index faceted Ni$_3$S$_2$ nanosheet arrays as highly active and ultrastable electrocatalysts for water splitting, J. Am. Chem. Soc. 137 (2015) 14023–14026.

[29] X.W. Ou, Z.T. Luo, One-step synthesis of Ni$_3$S$_2$ nanoplatelets on graphene for high performance supercapacitors, RSC Adv. 6 (2016) 10280–10284.

[30] Y.Y. Wu, G.D. Li, Y.P. Liu, L. Yang, X.R. Lian, T. Asefa, X.X. Zou, Overall water splitting catalyzed efficiently by an ultrathin nanosheet-built, hollow Ni$_3$S$_2$-based electrocatalyst, Adv. Funct. Mater. 26 (2016) 4839–4847.

[31] Z. Fang, Y.B. Wang, J.B. Song, Y.M. Sun, J.J. Zhou, R. Xu, H.W. Duan, Immobilizing CdS quantum dots and dendritic Pt nanocrystals on thiolated graphene nanosheets toward highly efficient photocatalytic H$_2$ evolution, Nanoscale 5 (2013) 9830–9838.

[32] Y.-X. Pan, H.Q. Zhuang, J.D. Hong, Z. Fang, H. Liu, B. Liu, Y.Z. Huang, R. Xu, Cadmium sulfide quantum dots supported on gallium and indium oxide for visible-light-driven hydrogen evolution from water, ChemSusChem 7 (2014) 2537–2544.

[33] Y.-X. Pan, T.H. Zhou, J.Y. Han, J.D. Hong, Y.B. Wang, W. Zhang, R. Xu, CdS quantum dots and tungsten carbide supported on anatase–rutile composite TiO$_2$ for highly efficient visible-light-driven photocatalytic H$_2$ evolution from water, Catal. Sci. Technol. 6 (2016) 2206–2213.

[34] Y.-X. Pan, J.B. Peng, S. Xin, Y. You, Y.L. Men, F. Zhang, M.Y. Duan, Y. Cui, Z.Q. Sun, J. Song, Enhanced visible-light-driven photocatalytic H$_2$ evolution from water on noble-metal-free CdS-nanoparticle-dispersed Mo$_2$C@C nanospheres, ACS Sustain. Chem. Eng. 5 (2017) 5449–5456.

[35] M.A.M. Vásquez, M. Hamer, N.I. Neuman, A.Y. Tesio, A. Hunt, H. Bogo, E.J. Calvo, F. Doctorovich, Iron and cobalt corroles in solution and on carbon nanotubes as molecular photocatalysts for hydrogen production by water reduction, ChemCatChem 9 (2017) 3259–3268.

[36] S. Nardecchia, D. Carriazo, M.L. Ferrer, M.C. Gutiérrez, F. del Monte, Three dimensional macroporous architectures and aerogels built of carbon nanotubes and/or graphene: synthesis and applications, Chem. Soc. Rev. 42 (2013) 794–830.

[37] X.N. Guo, C.H. Hao, G.Q. Jin, H.Y. Zhu, X.Y. Guo, Copper nanoparticles on graphene support: an efficient photocatalyst for coupling of nitroaromatics in visible light, Angew. Chem. Int. Ed. 53 (2014) 1973–1977.

[38] G. Yang, D. Gao, J. Zhang, Z. Shi, D. Xue, Evidence of vacancy-induced room temperature ferromagnetism in amorphous and crystalline Al$_2$O$_3$ nanoparticles, J. Phys. Chem. C 115 (2011) 16814–16818.

[39] Y.-X. Pan, C.J. Liu, D.H. Mei, Q.F. Ge, Effects of hydration and oxygen vacancy on CO$_2$ adsorption and activation on β-Ga$_2$O$_3$(100), Langmuir 26 (2010) 5551–5558.

[40] H.V. Thang, L. Grajciar, P. Nachtigall, O. Bludký, C.O. Areán, E. Frýdová, R. Bulánek, Adsorption of CO$_2$ in FAU zeolites: effect of zeolite composition, Catal. Today 227 (2014) 50–56.

[41] W.R. Lee, S.Y. Hwang, D.W. Ryu, K.S. Lim, S.S. Han, D. Moon, J. Choi, C.S. Hong, Diamine-functionalized metal–organic framework: exceptionally high CO$_2$ capacities from ambient air and flue gas, ultrafast CO$_2$ uptake rate, and adsorption mechanism, Energy Environ. Sci. 7 (2014) 744–751.

[42] G.P. Hao, Z.Y. Jin, Q. Sun, X.Q. Zhang, J.T. Zhang, A.H. Lu, Porous carbon nanosheets with precisely tunable thickness and selective CO$_2$ adsorption properties, Energy Environ. Sci. 6 (2013) 3740–3747.

[43] Y.-X. Pan, C.J. Liu, Q.F. Ge, Effect of surface hydroxyls on selective CO$_2$ hydrogenation over Ni$_4$/γ-Al$_2$O$_3$: a density functional theory study, J. Catal. 272 (2010) 227–234.

[44] Y.-X. Pan, C.J. Liu, T.S. Wiltowski, Q.F. Ge, CO$_2$ adsorption and activation over γ-Al$_2$O$_3$-supported transition metal dimers: a density functional study, Catal. Today 147 (2009) 68–76.

[45] A. Solis-Garcia, J.F. Louvier-Hernandez, A. Almendarez-Camarillo, J.C. Fierro-Gonzalez, Participation of surface bicarbonate, formate and methoxy species in the carbon dioxide methanation catalyzed by ZrO$_2$-supported Ni, Appl. Catal. B: Environ. 218 (2017) 611–620.

[46] S.A. Burgess, A.M. Appel, J.C. Linehan, E.S. Wiedner, Changing the mechanism for CO$_2$ hydrogenation using solvent-dependent thermodynamics, Angew. Chem. Int. Ed. 56 (2017) 15002–15005.

[47] H. Ooka, M.C. Figueiredo, M.T.M. Koper, Competition between hydrogen evolution and carbon dioxide reduction on copper electrodes in mildly acidic media, Langmuir 33 (2017) 9307–9313.

[48] Z. Sun, C. Zhang, L. Xing, Q. Zhou, W. Dong, M.R. Hoffmann, UV/Nitrilotriacetic acid process as a novel strategy for efficient photoreductive de gradation of perfluorooctanesulfonate, Environ. Sci. Technol. 52 (2018) 2953–2962.

[49] V. Pawar, S. Appari, D.S. Monder, V.M. Janardhanan, Study of the combined deactivation due to sulfur poisoning and carbon deposition during biogas dry reforming on supported Ni catalyst, Ind. Eng. Chem. Res. 56 (2017) 8448–8455.

[50] J.P. Feng, J.J. Liu, M.X. Tang, L.G. Zhou, X.Y. Zhang, X.D. Wen, H. Ge, D.B. Li, X.K. Li, Effect of sulfur–carbon interaction on sulfur poisoning of Ni/Al$_2$O$_3$ catalysts for hydrogenation, Int. J. Hydrogen Energy 42 (2017) 6727–6737.

[51] G. Garbarino, E. Finocchio, A. Lagazzo, I. Valsamakis, P. Riani, V.S. Escribano, G. Busca, Steam reforming of ethanol–phenol mixture on Ni/Al$_2$O$_3$: effect of magnesium and boron on catalytic activity in the presence and absence of sulphur, Appl. Catal. B: Environ. 147 (2014) 813–826.